Journal of Corrosion and Materials
www.corromat.com

J. Corros. Mater. (2023) 2(2), 128–141.

Electrochemical Limits for Chloride-Induced Corrosion of Reinforcing Steel in Slag-Rich, Slag/Fly Ash, and Fly Ash-Rich Alkali-Activated Mortars

A. P. S. Patrick Selvadurai[1,*]

[1] *Department of Civil Engineering and Applied Mechanics, McGill University, Montreal, Quebec H3A 0C3, Canada*

*Corresponding author: patrick.selvadurai@mcgill.ca

(Received: 12 September 2023. Received in revised form: 26 November 2023. Accepted: 13 December 2023. Published online: 30 December 2023.)

Abstract

Corrosion of reinforcing steel in alkali-activated mortars caused by chlorides involves effects on binder chemistry, chloride penetration behavior, pore solution conductivity, steel surface state, and corrosion kinetics. It is not possible to apply criteria used for Ordinary Portland cement to alkali-activated materials since slag rich, slag/fly ash blended, and fly ash rich mortars generate dissimilar levels of alkalinity in steel environment. The aim of this research was to investigate the corrosion state of reinforcing steel embedded in three types of alkali-activated mortars, SN3 (87.67 % mass blast furnace slag), BN3 (41.12 % mass blast furnace slag, 46.61 % mass fly ash), and FN9 (68.76 % mass fly ash). Reinforced mortars were tested either in tap water or in chloride environment with 8 h of spraying with 5 % wt NaCl solution, 24 h of storage under 100 % relative humidity, and drying for 24 h at 50 ± 4 °C. Corrosion potential, polarization resistance, electrochemical impedance spectroscopy, Tafel slopes, and gravimetric steel loss were considered as indicators of the corrosion status of steel bars. Mortar strength for SN3 was 47.6 MPa at 28 days, its total porosity 4.59 %, and chloride migration coefficient 1.64×10^{-12} m^{2}s^{-1}. In BN3 compressive strength after 28 days was equal to 39.8 MPa, the chloride migration coefficient being 2.20×10^{-12} m^{2}s^{-1}. FN9 reached strength of 25.9 MPa after 28 days and exhibited very high chloride migration coefficient of 174×10^{-12} m^{2}s^{-1}. The electrochemical response corresponded to this material sequence. Mortars of types SN3 and BN3 remained in passive state with low corrosion current density throughout the time of chloride exposure. Mortar FN9 reached corrosion current density of approximately 6 μAcm^{-2} after 40 days and 30 μAcm^{-2} near the end of the experiment. Fly ash rich mortar showed also very low mortar resistivity and early appearance of cracks. For the examined alkali-activated mortars, passive or negligible corrosion is indicated by $E_{\text{corr}} > -400$ mV versus SCE, $R_{\text{mortar}} > 80$ kΩ cm^2, $n > 0.6$, low i_{corr}, and $B = 15$–25 mV. Evidence of active corrosion was defined by $E_{\text{corr}} < -400\,mV$ vs. SCE, $R_{mortar} < 80$ kΩcm^{-2}, $n < 0.6$, increasing i_{corr}, concrete cracking or steel loss, and $B = 55$ to 63 mV. These limits show that potential must be interpreted with polarization resistance, impedance parameters, Tafel slopes, and physical damage evidence when diagnosing chloride corrosion in reinforced alkali-activated mortars.

Keywords: alkali-activated mortar; reinforcing steel; chloride corrosion; blast-furnace slag; fly ash; electrochemical impedance spectroscopy; Stern–Geary coefficient; polarization resistance.

1. Introduction

The corrosion of reinforcing steel bars due to chloride ions is one of the reasons for early degradation of reinforced concrete and mortar that comes into contact with marine spray, de-icing salts, tidal splash, coastal atmospheric humidity, or saline ground water. The present assessment follows reported corrosion parameters for steel in alkali-activated materials [1]. Classical service-life modelling explains why chloride ingress must be separated from later corrosion propagation [2]. Once corrosion sets in, iron dissolution, oxygen reduction, moisture migration, and product formation happen simultaneously. Comprehensive concrete-corrosion literature connects these reactions with cracking, debonding, cover damage, and steel section loss [3]. Critical chloride-content reviews show why depassivation thresholds cannot be treated as universal constants [4].

Steel passivation is typically achieved using the highly alkaline environment generated by hydration processes in ordinary Portland cement concrete. The high pH is due to calcium hydroxide and other alkali hydroxides, which create an environment wherein a thin film of iron oxide or oxyhydroxide forms on the reinforcing bars. Linear polarization resistance provides a quantitative route for estimating corrosion rate in reinforced concrete [5]. Long-term monitoring studies connect corrosion rate with laboratory and field diagnosis [6]. Half-cell potential mapping is useful for locating areas with higher probability of reinforcement corrosion [7]. On-site polarization-resistance methods also show that corrosion-rate interpretation depends on test conditions and material environment [8]. Results obtained from one matrix therefore cannot be directly compared to those from another.

Reaction products, pore solution compositions, chloride binding properties, electrical conductivities, and redox activities vary between alkali-activated binders and Portland cement. Durability studies of alkali-activated materials identify binder chemistry as a central variable [9]. General alkali-activated-materials reviews similarly emphasize differences in reaction products and pore solution chemistry [10]. Round-robin testing shows that carbonation and chloride-penetration assessments

may vary with test protocol and binder type [11]. Slag-rich alkali-activated mortars and concretes can show reduced water and chloride permeability when the pore structure is refined [12]. Alkali-activated fly ash systems may display different chloride-penetration behavior because their reaction products and pore network differ from slag-rich systems [13]. Reviews of carbonation and chloride penetration further show that transport, binding, and pore solution chemistry must be interpreted together [14]. Slag-based mortars tend to exhibit low chloride diffusion and good steel corrosion resistance properties, while fly ash-based ones have relatively slow reactions and higher chlorides mobility or lower steel resistance when densification is poor.

Chloride threshold also varies depending on the type of binder used. Chloride can be considered in terms of total chloride, free chloride, bound chloride, water-soluble chloride, acid-soluble chloride, and chloride-to-hydroxyl ratio. The presentation of chloride threshold values can itself change the interpretation of corrosion risk [15]. Reviews of threshold levels show that moisture state, temperature, steel surface condition, oxygen availability, carbonation, and pore-solution alkalinity affect depassivation [16]. Reinforced alkali-activated mortars further show that calcium, alkali, and silicate contents influence chloride diffusivity and corrosion initiation [17]. Chloride binding in alkali-activated mortars is therefore based on different chemical mechanisms than in the case of ordinary Portland cement paste. Hence, a threshold of chloride transfer will not be a good criterion for predicting corrosion.

The presence of slags in alkali-activated binders provides an extra redox reaction due to the possibility of sulfur in a reduced state, which may affect the potential of steel. Simulated pore-solution studies show that chloride-induced corrosion in alkali-activated concretes can be affected by sulfide-containing alkaline chemistry [18]. Slag-composition studies confirm that steel stability depends on the chemistry of the alkali-activated cementitious environment [19]. Passivation mechanisms in sulfide-containing alkaline solutions further explain why negative steel potentials do not always mean high corrosion rate [20]. Chloride-transport studies in alkali-activated slag concretes connect ingress behavior with reinforcement corrosion response [21]. Alkali-activated mortars based on different precursors also show precursor-dependent chloride-induced corrosion behavior [22]. Simulated marine exposure confirms that low-carbon steel reinforcement can respond differently in alkali-activated slag-steel slag and Portland-cement mortars [23]. Long-term marine exposure studies demonstrate that alkali-activated slag mortar can provide sustained corrosion resistance when its pore structure remains favorable [24]. Carbonated alkali-activated slag concrete has also shown distinctive steel-corrosion behavior compared with ordinary cement systems [25]. Therefore, a negative potential is not indicative of fast corrosion reaction; instead, it is associated with the redox reactions, oxygen depletion, or film formation on steel surfaces.

Polarization resistance contains information regarding rate as well since it is defined by the tangent of the slope of the potential-current curve at the corrosion potential with respect to the corrosion current density. The polarization-resistance approach is a classical basis for reinforced-concrete corrosion-rate measurement [5]. Theoretical analysis also shows that polarization-resistance measurements must be interpreted through the electrochemical condition of steel in concrete [26]. For Portland cement mixes, monitoring studies commonly use Stern–Geary coefficients in the range of approximately 26 to 52 mV depending on the steel status [6]. However, when using alkali-activated materials, this value may vary since it relies on properties of iron oxidation, oxygen reduction, chloride activity, passive film formation, and surface area that are influenced by the binder.

Electrochemical Impedance Spectroscopy offers further differentiation between the set mortar and the steel surface. The high-frequency resistance, R_{mortar}, accounts for the ionic conductance in the mortar and pore solution. Concrete-resistivity literature shows that bulk resistance and corrosion rate must be read together rather than treated as identical quantities [27]. On-site resistivity recommendations also support the use of resistivity as a condition indicator rather than a complete corrosion diagnosis [28]. The low-frequency behavior corresponds to the steel-solution interface by means of charge transfer resistance and the constant phase element n. Constant-phase-element analysis provides the basis for interpreting nonideal capacitive response [29]. Electrochemical impedance theory further supports separating solution resistance, charge-transfer resistance, and interfacial dispersion [30]. If n is close to unity, then the surface is relatively uniform; lower values correspond to localized corrosion, the formation of corrosion products, uneven wetting, and film breakdown.

The investigation evaluates electrochemical thresholds for reinforcement bars in three chemically distinct types of alkali-activated mortars. The first is SN3 (high slag), second BN3 (slag-fly ash blend) and third FN9 (high fly ash). This work correlates chemistry of precursors, composition of the mortars, compressive strength, porosity, chloride ingress, chloride permeability, potential difference, polarization resistance, impedance behavior, Tafel slopes and mass loss of steel. The primary issue at stake here is whether it would be possible to classify these three mortars according to either passive or active state of corrosion based on their potential, resistance, interface behavior, corrosion current and steel loss readings. The approach to obtaining the result is based on the careful measurement of the response of SN3, BN3, and FN9 samples subjected to tap water and cyclic chloride attacks.

2. Materials and Methods

2.1 Starting materials and activation solution

Ground granulated blast furnace slag, BFS_E, and siliceous fly ash, FA_P, were used as the sources of aluminosilicates. BFS_E consisted of 31.1 wt.% SiO_2, 13.7 wt.% Al_2O_3, 40.9 wt.% CaO, 9.2 wt.% MgO, 2.3 wt.% SO_3, and iron oxide 0.4 wt.%. FA_P consisted of 57.2 wt.% SiO_2, 25.1 wt.% Al_2O_3, 5.8 wt.% Fe_2O_3, 4.8 wt.% CaO, 1.5 wt.% K*2O, and 1.1 wt.% Na*2O. The structure of BFS_E was completely amorphous according to the X-ray analysis. FA_P was found to be composed of 66.8% amorphous compounds in conjunction with the formation of various crystalline compounds such as mullite, quartz, anhydrite, magnetite, and free lime. The average particle size, represented by $D*v,0.5$, of BFS_E was measured to be 4.9 μm, whereas FA_P had a higher value of $D*v,0.5 = 11.5$ μm. Microstructural analysis of cementitious materials provides the methodological background for relating precursor chemistry and particle features to hardened-mortar behavior [31]. The activator was produced through a solution of sodium silicate having a modulus $M\_s = 1.68$ along with a 12.5 M solution of sodium hydroxide.

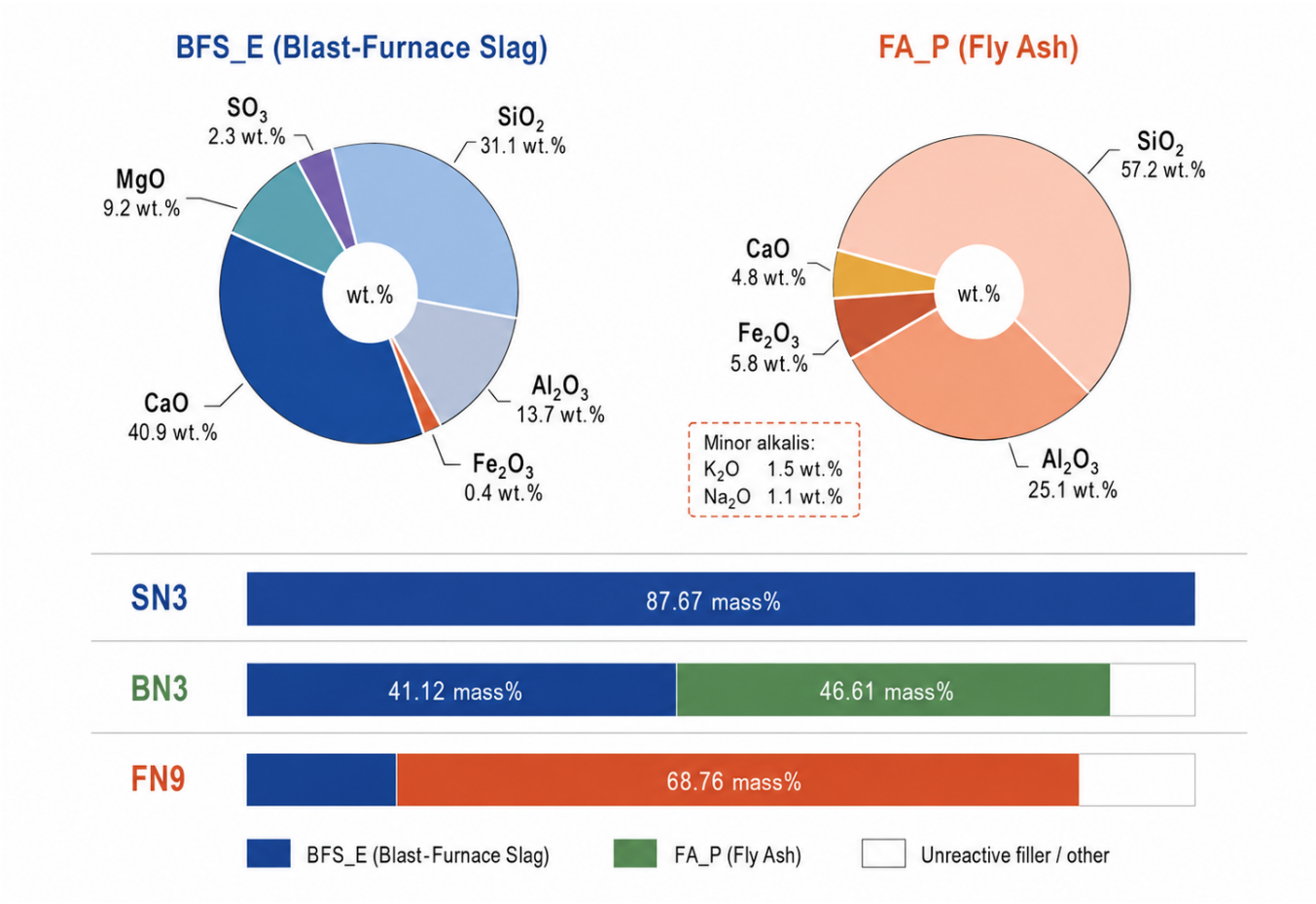

Figure 1: Oxide composition of the BFS_E slag and FA_P fly ash precursors, together with the binder fractions used in SN3, BN3, and FN9.

Composition-wise, it can be seen from Figure 1 that the slag precursor composition included more calcium containing glasses, but fly ash contained relatively high amounts of silicon and alumina. BFS_E had a smaller particle size, thus faster reaction rates, but FA_P was characterized by larger particle size and higher crystal content, which resulted in slower reaction rates. All these differences have an important role to play in terms of corrosion behavior due to their effect on pore refinement, movement of chlorides, pore solution chemistry, and stability of steel surfaces. Thus, SN3 is a slag-controlled binder, BN3 contains both slag and fly ash chemistry, and FN9 is fly ash-controlled.

2.2 Composition of mortar specimens and their transport properties

Three mortars were prepared from dolomite sand having grain size 0–4 mm. The water-to-binder ratio for all mortars was 0.45 and the ratio between the precursor and aggregate masses was 0.33. The composition of SN3 is 87.67 mass% BFS_E, 7.01 mass% NaOH, and 5.31 mass% sodium silicate. The composition of BN3 is 41.12 mass% BFS_E, 46.61 mass% FA_P, 7.02 mass% NaOH, and 5.25 mass% sodium silicate. The mixtures were selected to produce slag-rich, slag/fly ash, and fly ash-rich hardened mortars with distinct chloride-transport and steel-interface conditions.

Table 1: Composition and durability descriptors of the reinforced alkali-activated mortars.

Mixture	Binder type	BFS_E (mass%)	FA_P (mass%)	f_c at 28 d (MPa)	Porosity (%)	D_{mig} (10^{-12} m^2 s^{-1})
SN3	Slag-rich	87.67	–	47.6	4.59	1.64
BN3	Slag/fly ash	41.12	46.61	39.8	18.19	2.20
FN9	Fly ash-rich	–	68.76	25.9	13.90	174

Based on the results in Table 1, it is evident that SN3 mortar had the highest compressive strength after 28 days and the lowest chloride migration coefficient. Although BN3 mortar was found to be more porous compared to SN3 mortar, it still retained a chloride migration coefficient near to the mortar containing slag. In addition, the chloride migration coefficient in mortar FN9 was about two orders of magnitude higher compared to that in mortar SN3 and BN3. These differences indicate that steel in FN9 was exposed to a much more chloride-accessible and electrically conductive mortar body than steel in the slag-bearing mortars.

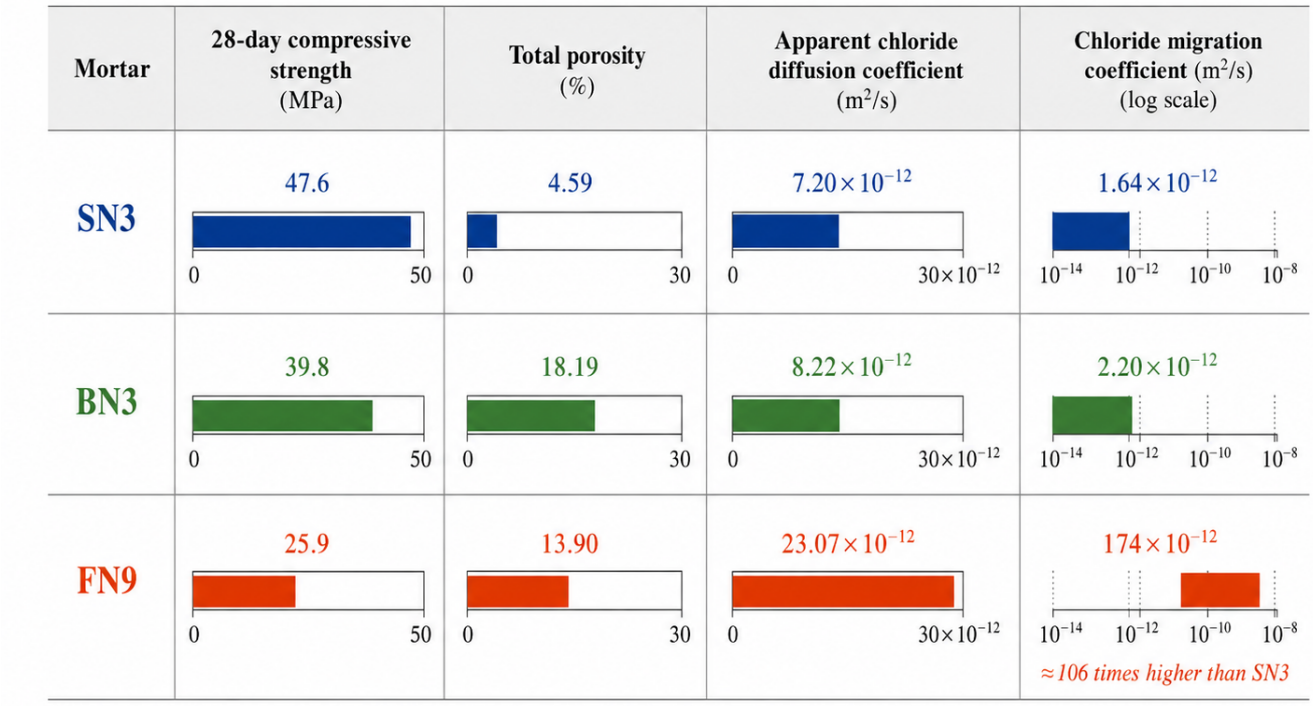

Figure 2: Strength, porosity, chloride diffusion, and chloride migration properties of SN3, BN3, and FN9.

From the above comparison, it can be seen that chloride permeability is more effective at distinguishing mortar FN9 from the other two mortars compared to the compressive strength and porosity. Although BN3 had a high percentage of fly ash, it only achieved a migration coefficient of 2.20×10^{-12} m^2 s^{-1}, which is close to SN3, with its migration coefficient of 1.64×10^{-12} m^2 s^{-1}. The value of FN9 was 174×10^{-12}m^{2}s^{-1}, which suggests that its pore structure offered a higher degree of ease in moving the chlorides. Hence, the higher mobility of chlorides can explain its faster corrosive response in the subsequent part of this study.

2.3 Reinforced specimens and method of exposure

Mortar samples were freshly molded using plastic molds having a diameter and height of 5 and 10 cm, respectively. A steel rod, whose dimensions are 0.6 cm and 8 cm for the diameter and height, respectively, was placed centrally in each mold. The steel was polished using 400, 600, and 800 grit size SiC paper and then washed with citric acid followed by drying with ethanol. Then, it was linked to the copper wire and sealed at the point of linking.

For 28 days after curing, three samples per mortar were immersed in tap water (21 ± 3 °C). Three more samples per mortar were subjected to chlorides attack under cyclic conditions in the salt spray chamber, which involved spraying the specimens with 5 wt.% of sodium chloride solution (20 ± 4 °C) for 8 hours, holding the sample in 100 % relative humidity (20 ± 4 °C) for 24 hours, and exposing the specimen to air (50 ± 4 °C) for another 24 hours. Other specimens were corroded under electric potential to have steel surfaces at various corrosion stages for subsequent Tafel analysis. Voltage of 5 V was applied to SN3 and BN3 specimens for 60 h and 140 h, respectively. Voltage of 3 V was applied to FN9 for 9 h and 30 h, respectively. The current density was kept below 200 μA cm^{-2}.

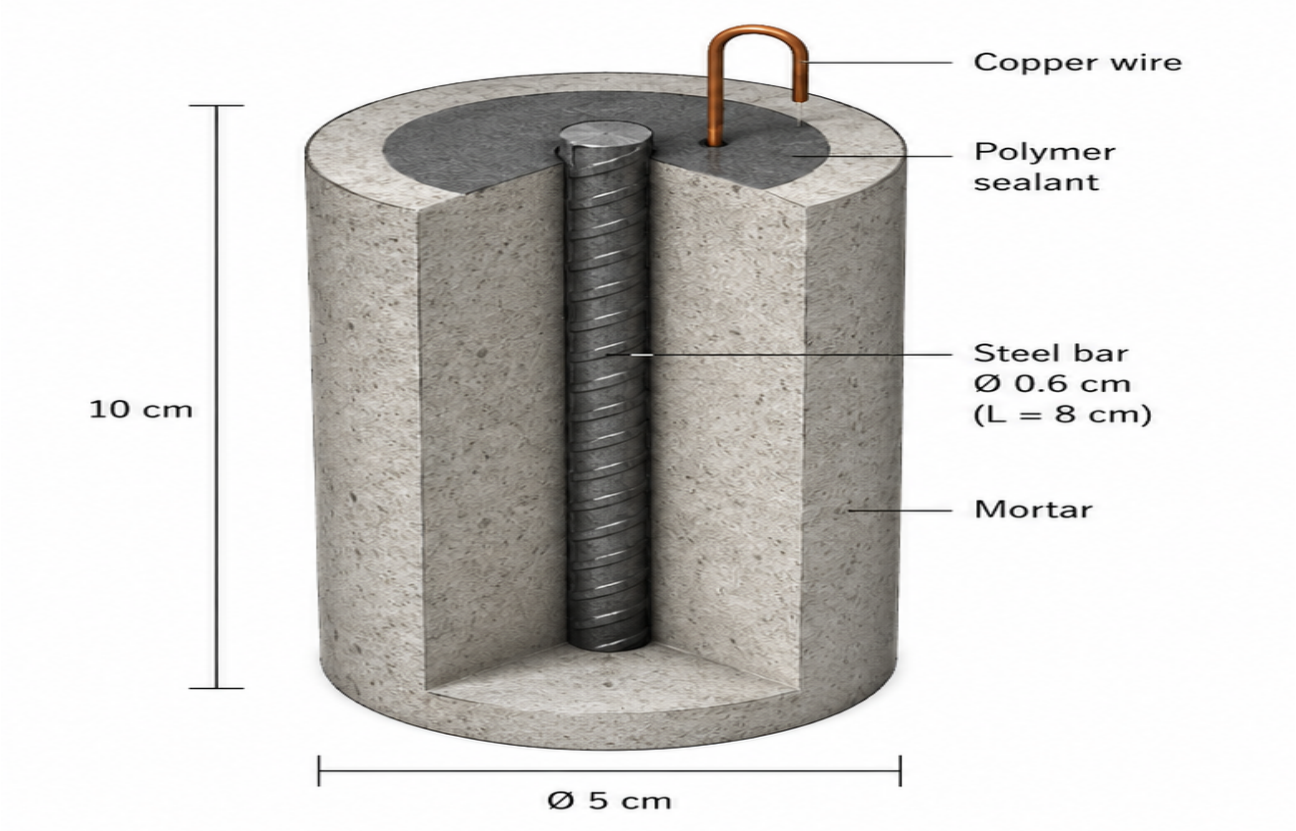

Figure 3: Reinforced mortar specimen geometry and exposure conditions used for the tap-water and chloride wet-dry tests.

Specimen configuration shown in Figure 3 consists of the steel placed at the center of a reinforced small mortar cylinder. In this way, electrochemical behavior was measured from the steel-mortar interface developed using the binders. Cyclic exposure of chloride involved chloride application, exposure time for humidity and drying. Chloride exposure at the specimen surface was done by spraying; humidity helped maintain continuous moisture whereas drying resulted in the concentration of the pore solution as well as increased oxygen availability.It was possible, under these circumstances, to compare the transport of Cl^-, depassivation, and corrosion propagation in SN3, BN3, and FN9.

2.4 Electrochemical tests

A three-electrode cell was utilized in all electrochemical tests. The steel that was embedded was the working electrode, while the counter electrode was represented by the graphite rod, and the saturated calomel electrode was the reference electrode. Open circuit potential was recorded for 15 min before measuring polarization resistance. Corrosion-potential testing of uncoated reinforcing steel in concrete provides the relevant standard reference for interpreting potential measurements [32]. Polarization resistance test was performed by biasing the steel ±10 mV around E_{corr}, with a sweep rate of 0.166 mV s^{-1}. The corrosion current density was obtained using the following Stern–Geary relation:

$$i_{\text{corr}} = \frac{\beta_a \beta_c}{2.3 R_p (\beta_a + \beta_c)} = \frac{B}{R_p}, \tag{1}$$

where R_p stands for polarization resistance, β_a and β_c are the anodic and cathodic Tafel slopes, respectively, and B is the Stern-Geary constant. For equation (1) to provide a correct corrosion current, B must reflect the real anodic and cathodic behaviour of steel within the mortar. Thus, Tafel tests were carried out in order to determine the values of B in its active and passive regions.

The electrochemical impedance spectroscopy study was carried out from 1 MHz down to 1.58 mHz at open circuit potential with an AC modulation of ±10 mV and five data points per decade. Spectra were analyzed by fitting with a circuit comprising mortar resistance (R_{mortar}) in series with a branch of the steel/electrolyte interface made up of charge transfer resistance (R_{ct}) and a constant phase element (CPE_{dl}). The constant-phase element impedance was expressed as

$$Z_{\text{CPE}} = [CPE(j\omega)^n]^{-1}, \tag{2}$$

where n is indicative of how far the system is away from ideal capacitors. The value of n closer to unity implies a homogeneous surface, while smaller values imply a heterogeneous surface due to localized corrosion, corrosion products, and poor wetting.

Tafel slopes were measured through potentiodynamic polarization tests at overpotentials of ±200 mV and sweep rates ranging from 2.5 mV min^{-1} to 10 mV min^{-1}. Post electrochemical testing, the specimens were cut, and the steel bars were subjected to cleaning in accordance with ASTM G1-03 standards [33]. Hydrochloric acid (1000 mL), stibium oxide (20 g), and stannum chloride (50 g) made up the cleaning mixture. The bars were brushed, dried, and weighed repeatedly until stable mass-loss values were obtained.

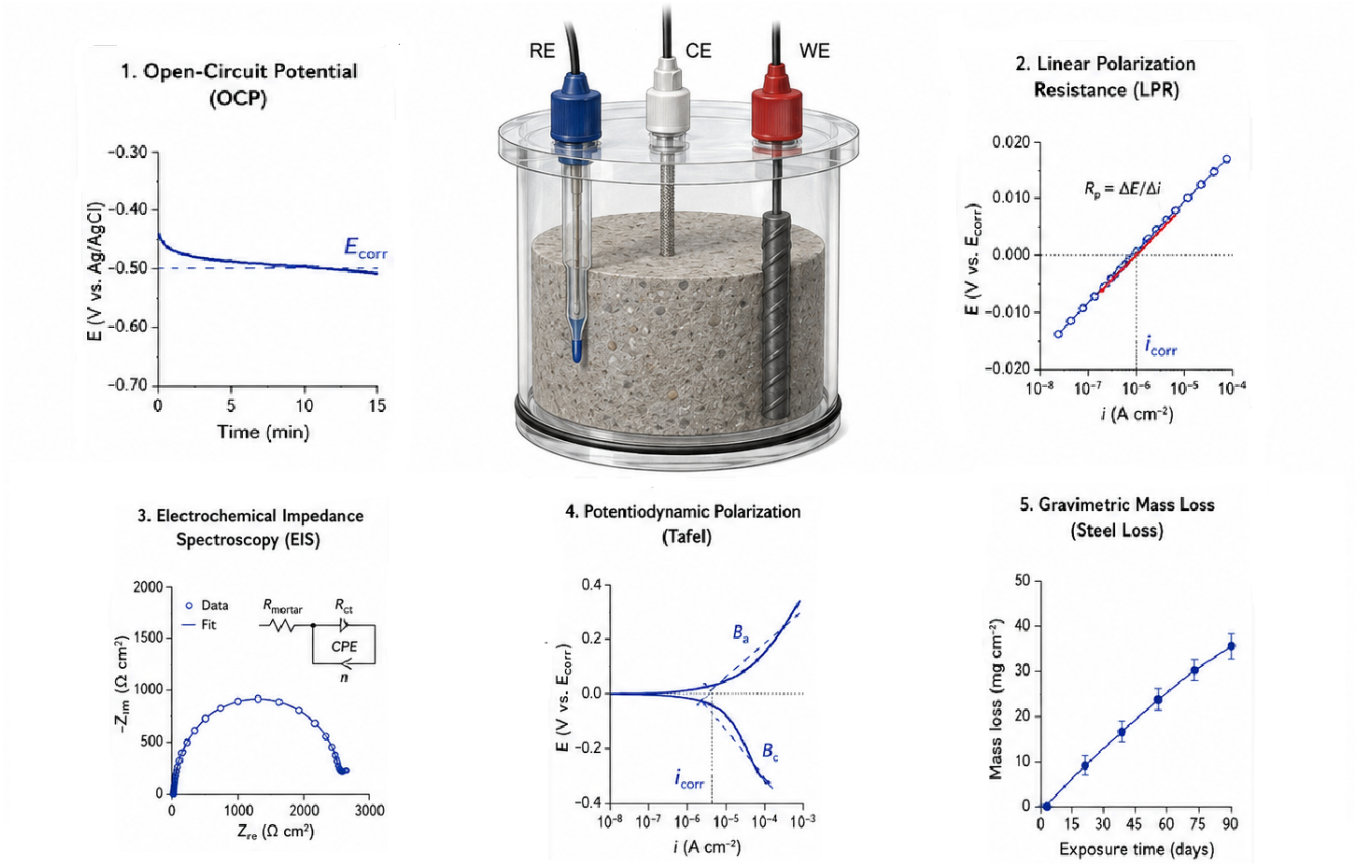

Figure 4: Electrochemical measurements used to obtain potential, polarization resistance, impedance parameters, Tafel slopes, and gravimetric steel loss.

The sequence of measurements presented in Figure 4 explains why the condition of corrosion was not established from one measurement. The potential of OCP measured the state of the mixed potential of the steel. The LPR yielded the rate-dependent polarographic response. The EIS isolated the resistance of the mortar from that of the steel-electrode branch. The potentiodynamic polarization yielded the Tafel slope and hence the value of B. Gravimetric cleaning checked whether the electrochemical estimate was consistent with physical steel loss.

Corrosion penetration depth was calculated as

$$P_{\mathrm{corr}} = \frac{11.6\, i_{\mathrm{corr}} t}{365}, \tag{3}$$

where P_{corr} is expressed in μm, i_{corr} in μA cm^{-2}, and t in days. This relation converts measured corrosion current into accumulated steel penetration and allows comparison between electrochemical activity and gravimetric steel loss.

3. Results and Discussion

3.1 Material properties and chloride movement

There were significant differences between the three mortars with regard to the transport characteristics prior to consideration of their behavior in the electrochemical test. The maximum compressive strength achieved by SN3 after 28 days was 47.6 MPa, while its total porosity was 4.59% with a migration coefficient of 1.64×10^{-12} m^2 s^{-1}. For BN3, the maximum compressive strength was 39.8 MPa, with total porosity of 18.19% and a migration coefficient of 2.20×10^{-12} m^2 s^{-1}. FN9 showed low compressive strength of just 25.9 MPa, with porosity and migration coefficient being 13.90% and 174×10^{-12} m^2 s^{-1} respectively. Apparent chloride diffusion coefficients for the hardened mortars also exhibited similar durability order, i.e., SN3 showed coefficient of 7.20×10^{-12} m^2 s^{-1}, while BN3 exhibited coefficient of 8.22×10^{-12} m^2 s^{-1}, whereas FN9 recorded a value of 23.07×10^{-12} m^2 s^{-1}.

Considering the fact that SN3 and BN3 possessed low chloride migration coefficients, it can be concluded that the slag contribution significantly inhibited the migration of chlorides. BN3 is significant because it consisted of fly ash with 46.61 mass% composition but still had migration coefficient value close to SN3.Hence, the slag content in BN3 was enough to provide chloride resistant hardened body for mortars. Such a large difference between the specimens is enough to justify that FN9 had fast potential shift, lower resistance mortar, higher corrosion current density and cracking.

Porosity itself cannot account for corrosion resistance of the samples. Mortar BN3 has the highest porosity (18.19%), but it is almost equal to that of specimen SN3 regarding chloride migration. However, FN9 has lower porosity than BN3; nevertheless, it has much higher chloride migration rate. It can be concluded that connectivity, pore size distribution, reactivity level and pore-solution chemistry have been more influential for corrosion resistance than porosity. For reinforced alkali activated mortars, corrosion protection is associated with formation of continuous ion pathways and chloride movement to the reinforcing steel.

Strength parameters are also consistent with the order of corrosion resistance. Specimen SN3 had the highest compression strength with the lowest chloride migration. Specimen BN3 has medium strength but good chloride resistance level. Finally, specimen FN9 has lower strength with extremely high chloride migration. Such combinations of properties make FN9 most susceptible to corrosion under wet dry cycling due to low mechanical and chloride resistance of hardened bodies.

3.2 Tap-water exposure - corrosion potential

In tap-water reference exposure, SN3 started out negative but reached an equilibrium value of −150 to −200 mV vs. SCE after approximately 60 days. BN3 changed around the value of −350 mV until approximately 250 days, when it began shifting towards positive values close to those of SN3 after long exposure times. FN9 equilibrated to a value around −400 mV within 70 days, and the test was terminated at approximately 150 days due to cracking.

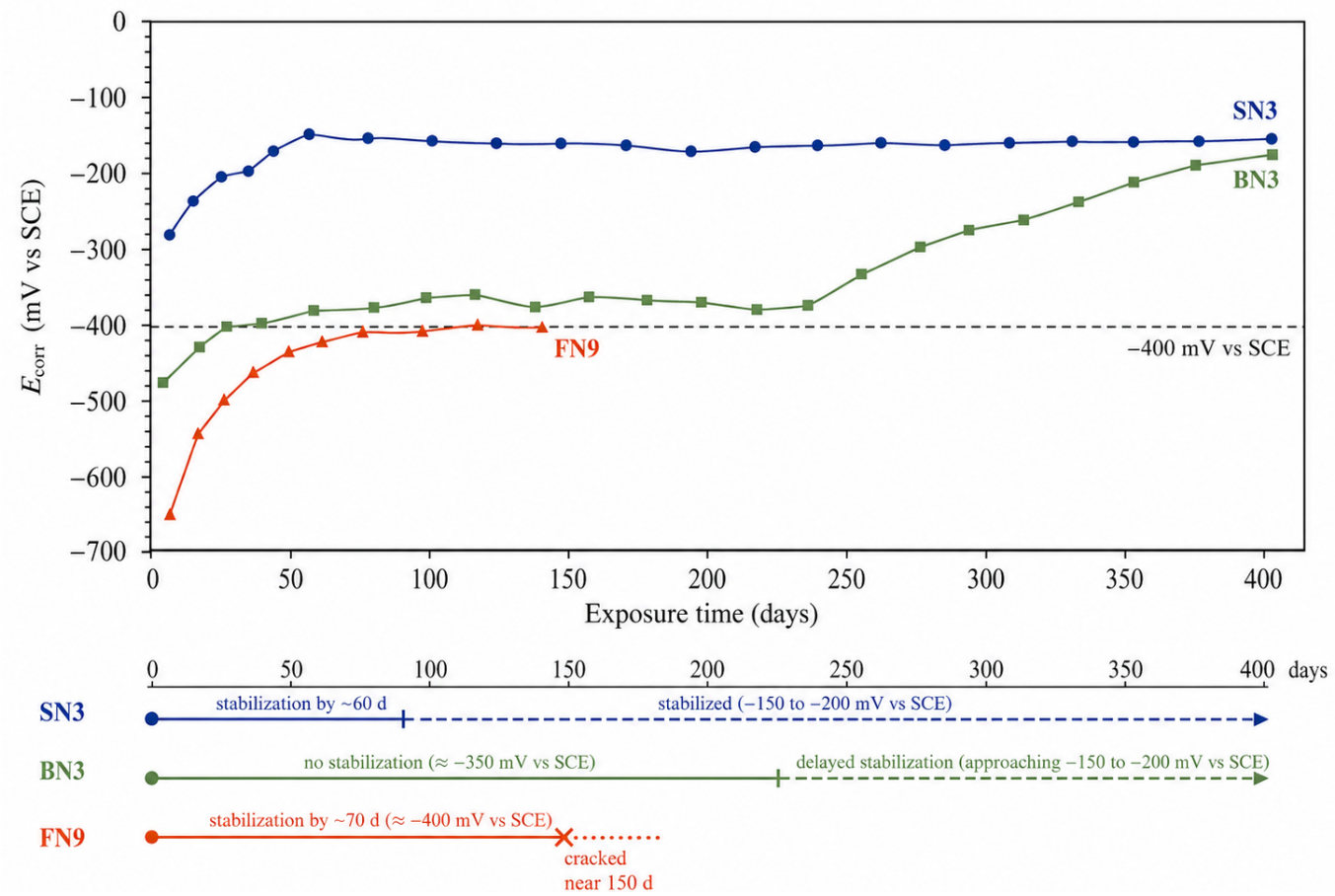

Figure 5: Corrosion potential of SN3, BN3, and FN9 under tap-water reference exposure.

In the case of tap water, Figure 5, the three types of binders did not create identical steel potentials in the absence of chloride ions. In particular, SN3 formed quite a stable passive potential. BN3 stayed quite negative for some time before moving in the direction of the SN3 results. The late change in potential indicates ongoing reactions resulting in the formation of more stable conditions for steel. FN9 stayed near the −400 mV mark and experienced cracking.

BN3 shows why the half-cell potential does not fully answer the question concerning the corrosion risks in alkali-activated mortars. With a potential near −350 mV vs. SCE, BN3 does not demonstrate as high a corrosion current density as FN9.

The reason for such a negative potential lies in the pore solution chemistry related to the use of slag materials. Thus, this type of potential required verification using the LPR technique and impedance testing.

Finally, there were differences in FN9 performance. This mortar created quite a high corrosion risk in the course of experiments since its potential remained within the corroding zone. Moreover, cracking appeared along with high corrosion current density. This way, for FN9, the negative potential corresponds to lower transport resistance.This difference between BN3 and FN9 proves that the meaning of E_{corr} depends on the properties of the binders.

3.3 Corrosion potential with cyclic exposure to chlorides

During chloride wet-dry cycling, SN3 and BN3 tended to show lower (less negative) values up to approximately −200 mV and −250 mV respectively with respect to SCE at approximately 70 days exposure time. These initial behaviors suggest that the mortars with slag were not susceptible to chloride-induced degradation at the steel surface in the beginning. With longer exposure time, both samples showed higher (more negative) values and reached approximately −510 mV at 360 days. FN9 showed a faster degradation and reached −500 mV around 130 days.

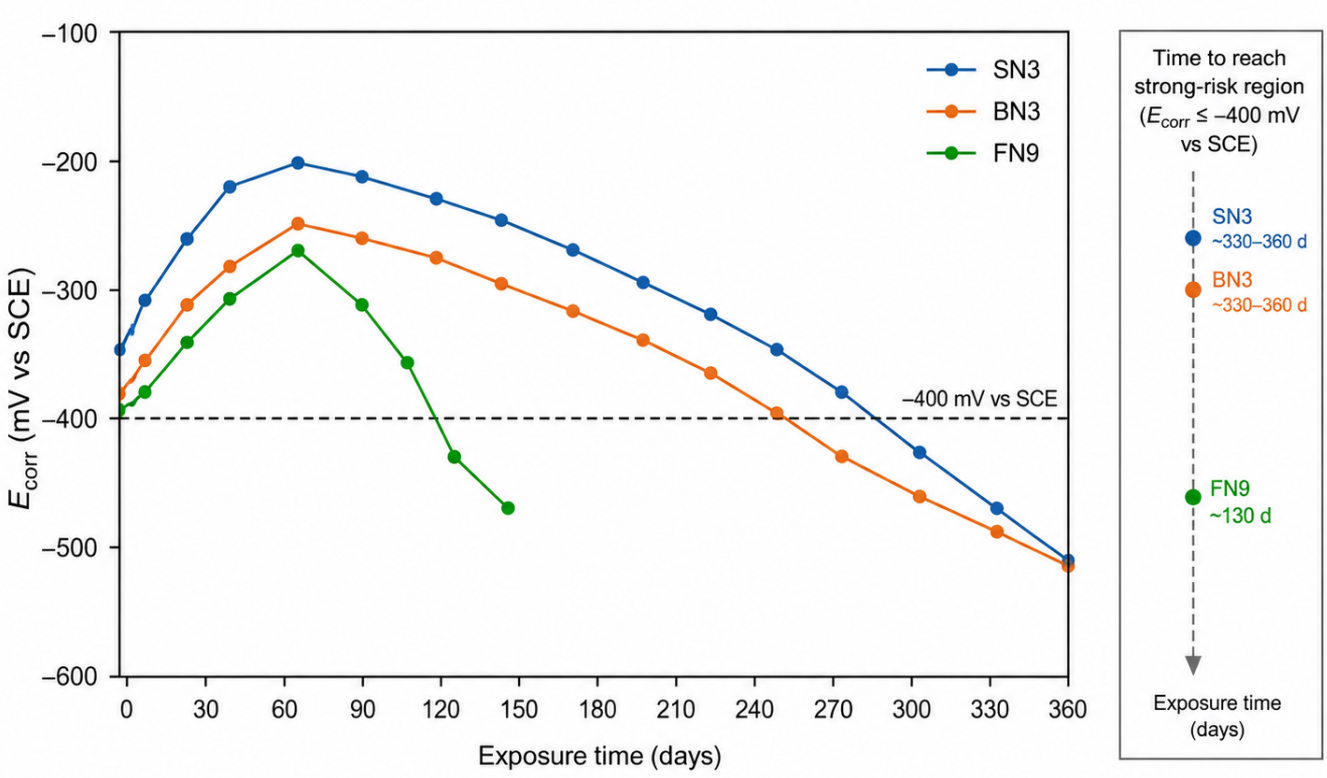

Figure 6: Corrosion potential of SN3, BN3, and FN9 under chloride wet-dry cycling.

The potential-versus-chloride exposure plots in Figure 6 display two different time regimes. SN3 and BN3 experienced the onset of negative potentials somewhat delayed, whereas FN9 reached strongly negative values quickly. It is related to a relatively small value of the migration coefficients for SN3 and BN3, and to very high values of this parameter and low resistivity for FN9. The transition of the potential below −400 mV thus was a more severe effect for FN9 than for slag-based mortars since in addition to it there were other symptoms of aggressive corrosion.

The delay in achieving −510 mV by SN3 and BN3 indicated that also the slag-based mortars may be affected by continuous wet-dry action of chlorides. Salt deposition, humidity and drying can accumulate chloride ions nearby steel bars, modify the access to oxygen, increase the electrochemical heterogeneity. It should be stressed that this kind of mortars' advantage was only the possibility to delay deterioration and decrease corrosion rates in most part of the testing period.

Thus potential values served as early warnings rather than final corrosion classifications. Potential values below −400 mV were considered significant when there were also low values of R_{mortar}, low values of n, high i_{corr} and presence of cracks or losses of steel. This phenomenon was especially pronounced in FN9.

3.4 Corrosion current density

The difference between the materials was evident when using corrosion current density as the criterion. SN3 and BN3 were below 0.2 $\mu\mathrm{A\,cm^{-2}}$ when exposed to tap water and below 0.4 $\mu\mathrm{A\,cm^{-2}}$ during much of the chloride exposure test period. Corrosion current density rose sharply in the case of FN9. Under chloride exposure, it reached approximately 6 $\mu\mathrm{A\,cm^{-2}}$

after 40 days and approximately 30 μA cm^{-2} near the end of testing. In tap-water exposure, FN9 approached approximately 40 μA cm^{-2} after 160 days.

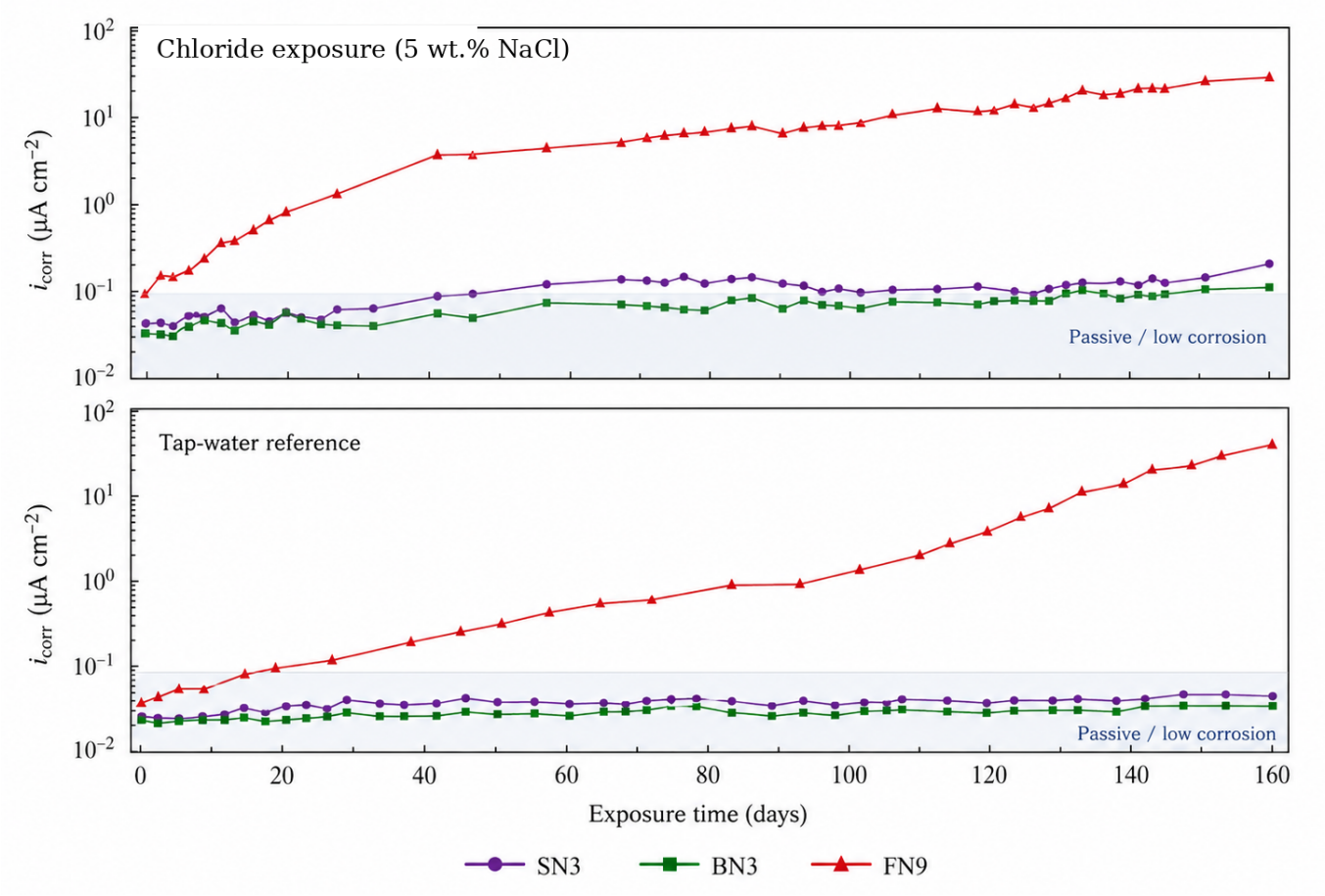

Figure 7: Corrosion current density of SN3, BN3, and FN9 under chloride cycling and tap-water reference exposure.

As observed from the current-density plots presented in Figure 7, both SN3 and BN3 retained a kinetic inhibition even after changes in potential values due to exposure. The steel surface did not corrode rapidly through most of the chloride exposure period. For FN9, corrosion occurred within the range of anodic corrosion current indicative of active steel loss. This distinction is crucial since E_{corr} refers to the electrochemical potential while i_{corr} refers to the rate of metal dissolution.

The fast rise of current density is explained by the properties of the material. As mentioned above, the fly ash-based binder had the highest chloride migration rate, low resistance to chloride migration, and premature cracking. Such characteristics facilitated fast corrosion reactions with the aid of moisture, oxygen, and chloride ions. In other words, once the cracks appeared, it becomes easier for the transport to reach the steel surface.

Low current density recorded by SN3 and BN3 suggests that the corrosion process was inhibited for a long time by the slag-rich binder materials. As before, BN3 demonstrates a remarkable property in the fact that fly ash did not cause such results as for FN9. The material composition consisted of 41.12 mass% slag and 46.61 mass% fly ash. Despite the higher ratio, the results are low chloride migration and i_{corr}. These findings confirm the suitability of using slag/fly ash binders in reinforced chloride-exposed environments when transport properties are established.

3.5 Steel-Interface Response

Separation was made between high frequency resistivity of the mortar and the low frequency response of the steel interface. R_{mortar} denoted the ionic resistance of the hardened mortar and pore solution. R_{ct} and CPE_{dl} denoted the charge-transfer resistance and capacitance behavior on the steel surface, respectively. A large value of R_{mortar} implies a poor ionic conductivity within the mortar, whereas the steel interface branch reflects if the steel surface is homogeneous or non-uniform. Separation was critical for alkali activated mortar, where there is a possibility of changing steel potential without inducing the same rate of corrosion in the absence of conductive pore solution.

SN3 and BN3 developed high values of R_{mortar} in tap water immersion due to the maturation process of the hardened material. In chloride solutions, both SN3 and BN3 showed an initial increase, reaching approximately 268 kΩ cm^2 and 253 kΩ cm^2, respectively. Late values approached approximately 55 kΩ cm^2 for SN3 and 66 kΩ cm^2 for BN3. FN9 remained near 1 kΩ cm^2 throughout testing.

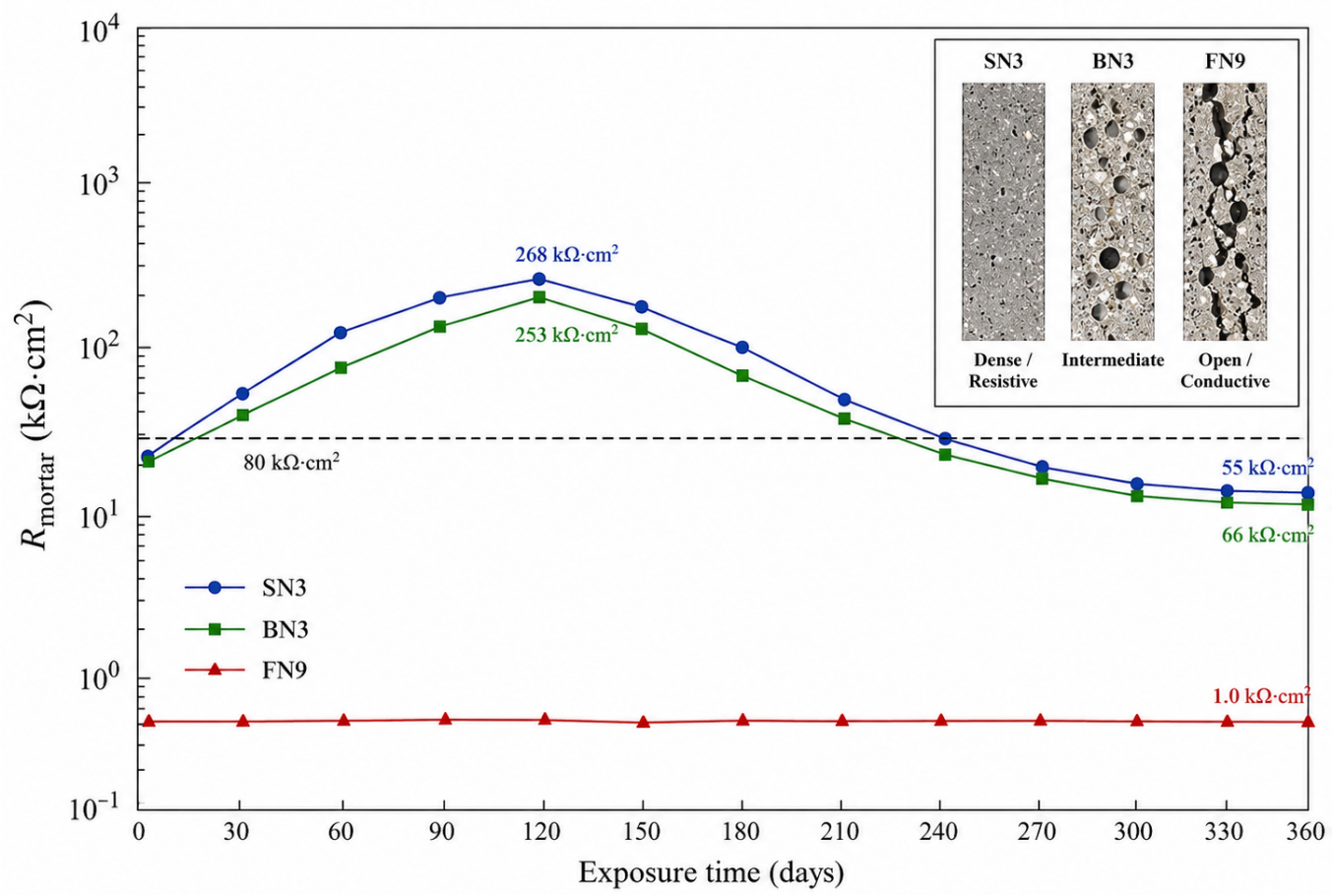

Figure 8: EIS-derived mortar resistance during chloride exposure.

The resistance behavior of Figure 8 is consistent with corrosion rates varying over time. The initially high resistances of SN3 and BN3 suppressed ionic migration, keeping the rate of steel dissolution low; their gradual reduction suggested increasing conductivity due to chloride wetting and drying, deposition of salts, damage, and product generation. Resistance of FN9 was low to begin with and never changed significantly; thus, the steel was immersed in electrolyte able to produce fast anodic and cathodic reactions.

The threshold value of resistance at 80 $k\Omega\,cm^2$ distinguished between the behavior of safe and potentially unsafe mortars. Resistances higher than this value were characteristic of SN3 and BN3 at low corrosion stage; those below this limit corresponded to FN9 and to the later stage of slag-containing mortars. Such a resistance value is significant in linking material transport processes to reaction kinetics.

Finally, the constant-phase index n carried additional information about the state of the steel surface. Higher values of n meant more homogenous capacitance interface. Lower n indicated distributed time constants as a result of roughness, corrosion products, local attack, and passive film breakdown. In conclusion, a combination of R_{mortar} and n characterized restrictions for ionic migration within the mortar and stability of the steel surface.

The state plot (Figure 9) shows that high R_{mortar} and $n > 0.6$ indicate passive or low corrosion activity. Conversely, low R_{mortar} and $n < 0.6$ represent active corrosion. The points for FN9 all fell into the active region, while SN3 and BN3 were within the low-corrosion region after early exposure but gradually approached the active region as their resistances decreased, and n became less than 0.6.

While a negative potential is possible in the slag-containing mortar with no high corrosion current, low resistance and low n value mean that changes occurred in both the mortar matrix and steel surface in favor of active corrosion. When these EIS parameters agree with increasing i_{corr}, then the correlation between them and corrosion process becomes much more certain.

3.6 Tafel slopes and Stern–Geary coefficient

It was found that the Stern–Geary coefficient depended on the state of corrosion. For the specimens with passive or low corrosion activities (BN3), the B value was around 15–16 mV. In the case of low corrosion activities of SN3, the B value was around 25–41 mV. In active corrosion cases of SN3 and BN3, the B value was approximately 50–64 mV. The B value of FN9 varied widely, i.e., 13.1 to 63.8 mV, due to rapid change of steel surface with increasing corrosion.

However, based on Figure 10, the Stern–Geary relation indicates that the value of one Portland cement for all the three

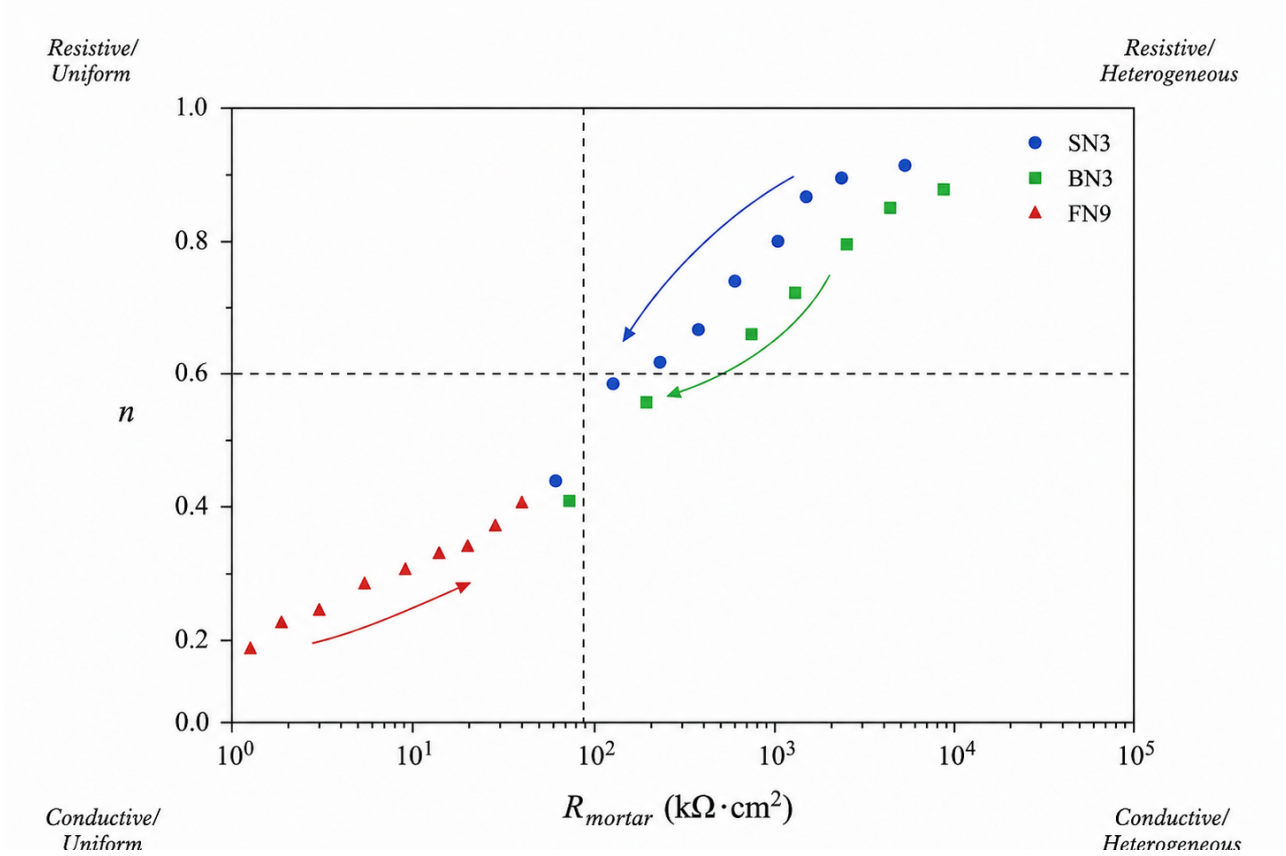

Figure 9: Relationship between mortar resistance and the constant-phase exponent of the steel-interface response.

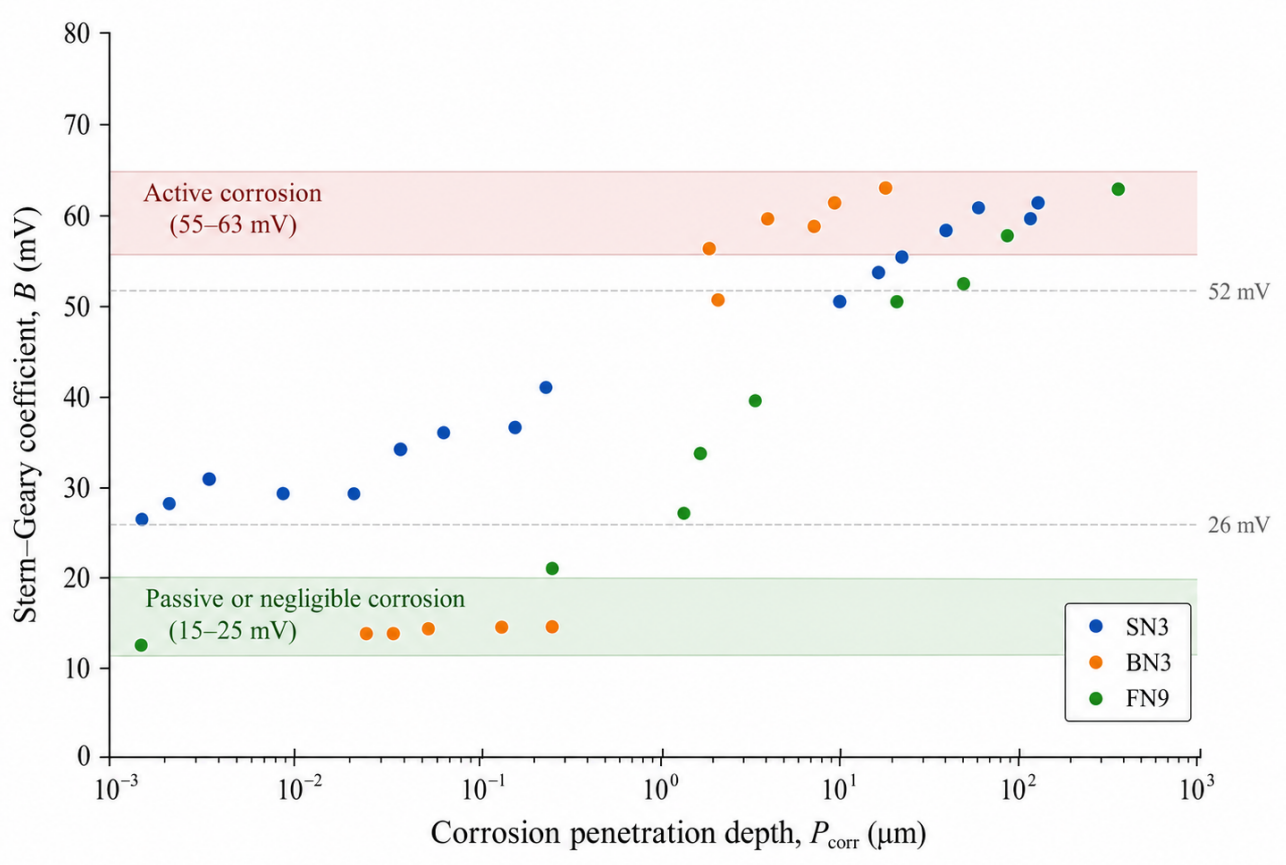

Figure 10: Stern–Geary coefficient as a function of corrosion penetration depth.

AAAs is not valid. Lower penetration depth means lower B value, since the surface of the steel stayed passive or slightly active. Higher penetration depth is correlated with higher B values since anodic dissolution, cathodic oxygen reduction, surface modification, and corrosion product film have impacted the Tafel slope.

The passive or slight corrosion was best characterized by using $B = 15$–25 mV. The active corrosion was best characterized by $B = 55$–63 mV. Assigning 26 mV to all passive samples will result in higher values for low corrosion activities, particularly for BN3. Assigning 52 mV to all active samples would underestimate the severity of the active steel condition seen in some sections of SN3, BN3, and FN9. The value of B should be decided from corrosion conditions rather than preassigned.

On the other hand, the penetration depth calculation provided the relationship between current density and accumulated steel dissolution. FN9 sample has achieved current density to create a detectable amount of penetration within a short time. On the other hand, SN3 and BN3 stayed in low current density (i_{corr}) for long periods of time. As a consequence, the penetration process took more time to occur. This correlation confirmed that FN9 was actively subjected to the dissolution process whereas SN3 and BN3 were mostly spared.

3.7 Corrosion limits in combination

The corrosion limits estimated from the experimentally recorded data are shown in Table 2. Both the limits need to be considered collectively. Just one limit is insufficient considering the changes in the chemistry of the binders as well as the conductance of pore solution.

Table 2: Electrochemical limits for the examined alkali-activated mortars.

Parameter	Passive or negligible corrosion	Active corrosion
E_{corr}	> -400 mV vs. SCE	< -400 mV vs. SCE
R_{mortar}	$> 80\ \text{k}\Omega\,\text{cm}^2$	$< 80\ \text{k}\Omega\,\text{cm}^2$
n	> 0.6	< 0.6
B	15–25 mV	55–63 mV
Confirmation	low i_{corr} and stable surface	rising i_{corr}, cracking, or steel loss

The results presented in Table 2 indicate that for corrosion classification it is essential to ensure agreement among potential, current density, impedance, Tafel slopes, and signs of damage. If potential is lower than -400 mV, there will not be any rapid corrosion processes in the presence of slag-bearing mortars provided current density is small and the surface of steel bars does not experience substantial changes. On the contrary, in FN9 mortar the same potential was accompanied by low impedance, low n, high current density, and cracking. The same potential therefore had different implications depending on the surrounding mortar and accompanying electrochemical evidence.

From the summary limit in Figure 11, the convergence of the different measurements towards the practical application is illustrated. E_{corr} reflects the electrochemical activity. R_p and i_{corr} represent the rate of steel dissolution. R_{mortar} shows the ions conducting through the hardened mortar. R_{ct} and n define the reactions at the steel surface and heterogeneity, respectively. B is the conversion factor from polarization resistance to corrosion current, taking into account the passive or active state. The gravimetric loss and cracking give physical evidence. By combining all this information, there would be less chance of misclassifying slag-dominated concrete as actively corroded because of negative potential or not considering fly ash-dominated specimens which are now in active corrosion stage.

SN3 had shown the highest resistance to corrosion due to the presence of high slag content, high strength, low porosity, low chloride migration, high mortar resistance, and low current density. BN3 exhibited delay in corrosion because of the slag/fly ash composition which ensured low chloride migration with low i_{corr}. FN9 was actively corroded as all indicators such as high chloride migration, low resistance, negative potential, high current density, low interfacial uniformity, and cracking were present simultaneously.

4. Conclusion

Chloride-induced corrosion of reinforcing steel in alkali-activated mortars relies heavily on precursor chemistry, chloride permeation kinetics, mortar durability, steel-surface heterogeneity, and the Stern-Geary coefficient applied for the conversion of polarization resistance into corrosion current density. Three studied mortars provided different responses due to their differing slag contents, fly ash contents, compressive strengths, porosities, and chloride diffusivities/migration coefficients.

With a slag content of 87.67 mass%, SN3 displayed a high durability level. It provided a compressive strength of 47.6 MPa in 28 days, 4.59% porosity, an apparent chloride diffusion coefficient of 7.20×10^{-12} m^2 s^{-1}, and a chloride migration

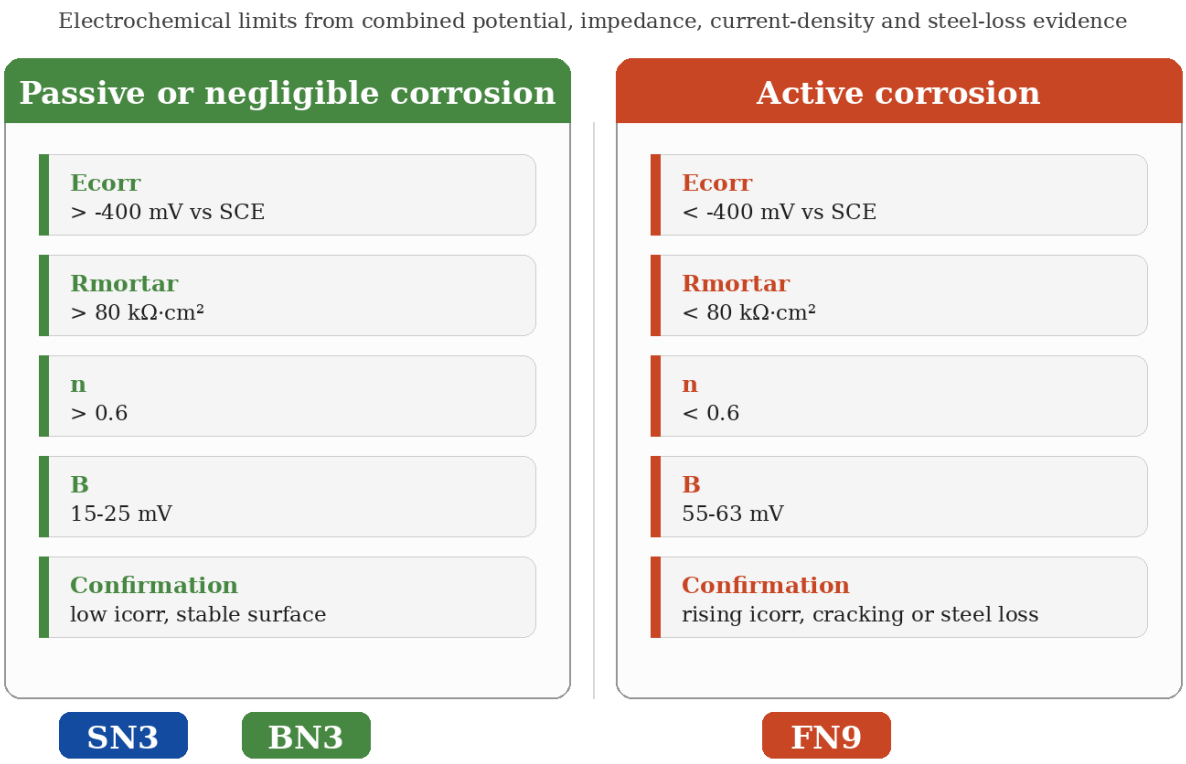

Figure 11: Final electrochemical limits for distinguishing passive or negligible corrosion from active corrosion in the examined alkali-activated mortars.

coefficient of 1.64×10^{-12} m^2 s^{-1}. High mortar resistance and low corrosion current density prevailed throughout the duration of chloride exposure. BN3, having 41.12 mass% slag and 46.61 mass% fly ash, was also durable enough to delay the start of corrosion. With a 18.19% porosity rate, its chloride migration coefficient remained as low as 2.20×10^{-12} m^2 s^{-1}, and its corrosion current density stayed low throughout most of the chloride exposure. However, in case of fly ash-based FN9 (68.76 mass% fly ash), corrosion of steel appeared to occur actively, with high chloride migration (174×10^{-12} m^2 s^{-1}), low mortar resistance, fast transition towards approximately -500 mV, corrosion current density of approximately 6 μA cm^{-2} by 40 days, approaching corrosion current density of 30 μA cm^{-2} at later stages of chloride exposure, and cracking of the mortar sample.

Limit of corrosion potential equaling -400 mV relative to SCE is valuable only in conjunction with another indicator. As shown previously, slags-containing mortars may display negative potentials, since reduction/oxidation chemistry is defined by sulfur reduction, oxygen accessibility, and redox state of the pore solution. Negative potentials lower than -400 mV become indicative of corrosion in case of simultaneous occurrence of $R_{\text{mortar}} < 80$ kΩ cm^2, $n < 0.6$, increasing i_{corr}, active-state B, cracking, and measured steel loss.

For investigated alkali-activated mortars, passive or negligible corrosion is indicated by $E_{\text{corr}} > -400$ mV relative to SCE, $R_{\text{mortar}} > 80$ kΩ cm^2, $n > 0.6$, $i_{\text{corr}} < 0.1$ μA cm^{-2}, and $B = 15 - 25$ mV. Active corrosion is indicated by $E_{\text{corr}} < -400$ mV relative to SCE, $R_{\text{mortar}} < 80$ kΩ cm^2, $n < 0.6$, increasing i_{corr}, presence of cracking/measurable steel loss, and $B = 55 - 63$ mV. These restrictions solve the problem of how to assess the corrosive condition based on the half-cell potential: diagnosing the condition of steel reinforcement in alkali-activated mortars must satisfy several criteria simultaneously: corrosion potential, polarization resistance, mortar resistance, interface behavior of the steel, B coefficient calculated via Tafel plots, and finally physical degradation signs.

Reinforced alkali-activated mortar must thus possess sufficient durability against chloride penetration as well as the stability of the steel interface. The two compositions based on slag (SN3 and BN3) were superior compared to that containing more fly ash (FN9) in terms of chloride transport resistance in the wetting/drying tests. Further development of the composition based on fly ash is necessary due to insufficient durability of reinforced mortars in chloride conditions.

Declaration of Competing Interest

The author declares no competing financial interest or personal relationship that could have influenced the preparation of this manuscript.

References

[1] Runci, A., Provis, J. L., & Serdar, M. (2023). Revealing corrosion parameters of steel in alkali-activated materials. Corrosion science, 210, 110849.

[2] Tuutti, K. (1982). Corrosion of steel in concrete.

[3] Bertolini, L., Elsener, B., Pedeferri, P., Redaelli, E., & Polder, R. B. (2013). Corrosion of steel in concrete: prevention, diagnosis, repair. John Wiley & Sons.

[4] Angst, U., Elsener, B., Larsen, C. K., & Vennesland, Ø. (2009). Critical chloride content in reinforced concrete—A review. Cement and concrete research, 39(12), 1122-1138.

[5] Andrade, C. G. J. A., & González, J. A. (1978). Quantitative measurements of corrosion rate of reinforcing steels embedded in concrete using polarization resistance measurements. Materials and corrosion, 29(8), 515-519.

[6] Andrade, C., & Alonso, C. (1996). Corrosion rate monitoring in the laboratory and on-site. Construction and building materials, 10(5), 315-328.

[7] Elsener, B., Andrade, C., Gulikers, J., Polder, R., & Raupach, M. (2003). Half-cell potential measurements—Potential mapping on reinforced concrete structures. Materials and Structures, 36(7), 461-471.

[8] Andrade, C., & Alonso, C. (2004). Test methods for on-site corrosion rate measurement of steel reinforcement in concrete by means of the polarization resistance method. Materials and structures, 37(9), 623-643.

[9] Bernal, S. A., & Provis, J. L. (2014). Durability of alkali-activated materials: progress and perspectives. Journal of the American Ceramic Society, 97(4), 997-1008.

[10] Provis, J. L. (2018). Alkali-activated materials. Cement and concrete research, 114, 40-48.

[11] Gluth, G. J., Arbi, K., Bernal, S. A., Bondar, D., Castel, A., Chithiraputhiran, S., ... & Provis, J. L. (2020). RILEM TC 247-DTA round robin test: carbonation and chloride penetration testing of alkali-activated concretes. Materials and Structures, 53(1), 21.

[12] Ismail, I., Bernal, S. A., Provis, J. L., San Nicolas, R., Brice, D. G., Kilcullen, A. R., ... & van Deventer, J. S. (2013). Influence of fly ash on the water and chloride permeability of alkali-activated slag mortars and concretes. Construction and Building Materials, 48, 1187-1201.

[13] Zhu, H., Zhang, Z., Zhu, Y., & Tian, L. (2014). Durability of alkali-activated fly ash concrete: Chloride penetration in pastes and mortars. Construction and Building Materials, 65, 51-59.

[14] Zhang, X., Long, K., Liu, W., Li, L., & Long, W. J. (2020). Carbonation and chloride ions' penetration of alkali-activated materials: a review. Molecules, 25(21), 5074.

[15] Glass, G. K., & Buenfeld, N. R. (1997). The presentation of the chloride threshold level for corrosion of steel in concrete. Corrosion science, 39(5), 1001-1013.

[16] Ann, K. Y., & Song, H. W. (2007). Chloride threshold level for corrosion of steel in concrete. Corrosion science, 49(11), 4113-4133.

[17] Babaee, M., & Castel, A. (2018). Chloride diffusivity, chloride threshold, and corrosion initiation in reinforced alkali-activated mortars: Role of calcium, alkali, and silicate content. Cement and Concrete Research, 111, 56-71.

[18] Mundra, S., Criado, M., Bernal, S. A., & Provis, J. L. (2017). Chloride-induced corrosion of steel rebars in simulated pore solutions of alkali-activated concretes. Cement and Concrete Research, 100, 385-397.

[19] Criado, M., Bernal, S. A., Garcia-Trinanes, P., & Provis, J. L. (2018). Influence of slag composition on the stability of steel in alkali-activated cementitious materials. Journal of materials science, 53(7), 5016-5035.

[20] Mundra, S., & Provis, J. L. (2021). Mechanisms of passivation and chloride-induced corrosion of mild steel in sulfide-containing alkaline solutions. Journal of materials science, 56(26), 14783-14802.

[21] Ma, Q., Nanukuttan, S. V., Basheer, P. M., Bai, Y., & Yang, C. (2016). Chloride transport and the resulting corrosion of steel bars in alkali activated slag concretes. Materials and Structures, 49(9), 3663-3677.

[22] Runci, A., & Serdar, M. (2020). Chloride-induced corrosion of steel in alkali-activated mortars based on different precursors. Materials, 13(22), 5244.

[23] You, N., Shi, J., & Zhang, Y. (2020). Corrosion behaviour of low-carbon steel reinforcement in alkali-activated slag-steel slag and Portland cement-based mortars under simulated marine environment. Corrosion Science, 175, 108874.

[24] Shi, J., Wu, M., & Ming, J. (2021). Long-term corrosion resistance of reinforcing steel in alkali-activated slag mortar after exposure to marine environments. Corrosion Science, 179, 109175.

[25] Aperador, W., De Gutiérrez, R. M., & Bastidas, D. M. (2009). Steel corrosion behaviour in carbonated alkali-activated slag concrete. Corrosion Science, 51(9), 2027-2033.

[26] Song, G. (2000). Theoretical analysis of the measurement of polarisation resistance in reinforced concrete. Cement and Concrete Composites, 22(6), 407-415.

[27] Hornbostel, K., Larsen, C. K., & Geiker, M. R. (2013). Relationship between concrete resistivity and corrosion rate–A literature review. Cement and concrete composites, 39, 60-72.

[28] Polder, R. B. (2001). Test methods for on site measurement of resistivity of concrete—a RILEM TC-154 technical recommendation. Construction and building materials, 15(2-3), 125-131.

[29] Brug, G. J., van den Eeden, A. L., Sluyters-Rehbach, M., & Sluyters, J. H. (1984). The analysis of electrode impedances complicated by the presence of a constant phase element. Journal of electroanalytical chemistry and interfacial electrochemistry, 176(1-2), 275-295.

[30] Orazem, M. E., & Tribollet, B. (2008). Electrochemical impedance spectroscopy. New Jersey, 1(906), 383-389.

[31] Scrivener, K., Snellings, R., Lothenbach, B., & Press, C. R. C. (Eds.). (2016). A practical guide to microstructural analysis of cementitious materials (Vol. 540). Boca Raton, FL, USA:: CRC press.

[32] Astm, C. (2015). Standard test method for corrosion potentials of uncoated reinforcing steel in concrete. ASTM International: West Conshohocken, PA, USA.

[33] ASTM, G. (2003). Standard practice for preparing, cleaning, and evaluating corrosion test specimens. In American Society for Testing and Materials.